Direct Observations of a Shock Traversing Preceding Two Coronal Mass Ejections: Insights from Solar Orbiter, Wind, and STEREO Observations

Yutian Chi[1] , Chenglong Shen[2,3] , Zhiyong Zhang[4], Mengjiao Xu[1] , Dongwei Mao[4], Junyan Liu[4] , Can Wang[4] ,
Bingkun Yu[1] , Jingyu Luo[4], Zhihui Zhong[4] , and Yuming Wang[2,3,5]

[1] Institute of Deep Space Sciences, Deep Space Exploration Laboratory, Hefei 230088, People's Republic of China
[2] Deep Space Exploration Laboratory/School of Earth and Space Sciences, University of Science and Technology of China, Hefei 230026, People's Republic of
China; clshen@ustc.edu.cn
[3] CAS Center for Excellence in Comparative Planetology, University of Science and Technology of China, Hefei, People's Republic of China
[4] CAS Key Laboratory of Geospace Environment, Department of Geophysics and Planetary Sciences, University of Science and Technology of China, Hefei, People's
Republic of China
[5] Anhui Mengcheng Geophysics National Observation and Research Station, University of Science and Technology of China, Mengcheng, Anhui, People's Republic
of China

Abstract

The three successive coronal mass ejections (CMEs) that erupted from 2023 November 27–28, provide the first opportunity to shed light on the entire process of a shock propagating through, sequentially compressing, and modifying two preceding CMEs using in situ data from Solar Orbiter, Wind, and STEREO-A. We describe the interaction of the three CMEs as follows: CME-1 and CME-2 interacted with each other at distances close to the Sun. Subsequently, the shock (S3) driven by CME-3 caught up with and compressed ICME-2 before 0.83 au, forming a typical shock–ICME interaction event observed by the Solar Orbiter. The S3 continued to propagate, crossing ICME-2 and propagating into ICME-1 as observed by Wind, and completely overtaking both ICME-1 and ICME-2 at STEREO-A. The interaction between S3 and the preceding two ICMEs leads to a clear compression of preceding ICMEs including an increase in magnetic field (~150%) and a reduction in the interval of ICMEs. It presents direct and compelling evidence that a shock can completely traverse two preceding CMEs, accompanied by a significant decrease in shock strength (magnetic compression ratio decrease from 1.74 to 1.49). Even though the three ICMEs interact significantly in the heliosphere, their magnetic field configurations exhibit coherence at different observation points, especially for ICME-3. Those results highlight the significant implications of shock–CME interactions for CME propagation and space weather forecasting.

Materials only available in the online version of record: animation

1. Introduction

Coronal mass ejections (CMEs) are dramatic plasma and magnetic field eruptions that carry mass and magnetic flux from the solar corona into the interplanetary medium. When the front of the CME exceeds the local fast magnetosonic speed in the solar wind frame, it can drive shocks, resulting in a discontinuity in plasma properties such as density, pressure, and velocity. During solar maximum, the eruption rate of CMEs can exceed 10 per day (S. Yashiro et al. 2004; N. Gopalswamy et al. 2005), making interactions between successive CMEs likely (N. Lugaz et al. 2017). Studies have shown that interacted CMEs, especially shock–ICME interactions, are more likely to induce intense geomagnetic storms compared to individual CMEs (L. F. Burlaga et al. 1987; Y. Wang et al. 2003a; C. Shen et al. 2017). The compression of the shock on preceding CMEs can significantly amplify the magnetic fields and velocities within ICMEs, which are critical parameters influencing their geoeffectiveness (C. Shen et al. 2017, 2018). As Solar Cycle 25 approaches its peak, we expect an increase in both the intensity of CMEs and the frequency of their interactions. A recent

example is the complex CME events that erupted between 2024 May 7 and 11. Multiple CMEs collided and merged during their propagation to Earth, forming a highly complexed structure when they reached 1 au. This interaction resulted in one of the most severe geomagnetic storms in over two decades, with a Dst_{min} of −411 nT, marking the strongest geomagnetic disturbance since 2003. This highlights the urgent need for a deeper understanding of the interaction processes between CMEs and shocks to better predict and mitigate the impacts of such powerful space weather events.

The interaction of successive CMEs can be observed remotely using radio emission data (N. Gopalswamy et al. 2001; M. Temmer et al. 2014) and white-light observations (N. Lugaz et al. 2009, 2012; Y. D. Liu et al. 2012), including coronagraphs and heliospheric imagers (HIs) on Solar TErrestrial RElations Observatory (STEREO; M. L. Kaiser et al. 2008). Although HIs reveal the evolution of density and kinematics (Y. D. Liu et al. 2012; C. Shen et al. 2012; W. Mishra et al. 2015; Y. Chi et al. 2021) in CME interactions, they can not provide information about the magnetic field. In situ data could provide direct insights into the CME–CME interaction process and the associated changes in plasma and magnetic field parameters (L. Burlaga 2002; Y. M. Wang et al. 2003b; C. Shen et al. 2017; C. Scolini et al. 2020). Fast magnetosonic forward shocks are typically identified by a

sudden enhancement in magnetic field strength, velocity, and plasma density. D. Trotta et al. (2023) investigated the properties of shocks and sheaths using multiple radially aligned spacecraft, observing several shocklets steepening in the relatively "quiet" upstream region of the shock. Following the shock, the ejecta part of a CME is determined by the enhanced magnetic field, a smooth changing magnetic field direction, a decrease in velocity, lower plasma density, and a reduced plasma β (the ratio of plasma pressure to magnetic pressure) (T. H. Zurbuchen & I. G. Richardson 2006; C.-C. Wu & R. P. Lepping 2011; Y. Chi et al. 2016). The region of compressed solar wind located between the shock front and the leading edge is referred to as the "sheath." Prior single-point in situ observations could only detect the results of CME–CME interactions rather than the entire interaction process (N. Lugaz et al. 2017). Consequently, direct observational evidence of the temporal evolution of the magnetic field during the interaction processes of CMEs is lacking. Understanding this evolution is crucial for improving space weather prediction models.

With the launch of the Solar Orbiter in 2020 (D. Müller et al. 2020), in situ observations of CME–CME interactions in the inner heliosphere have become feasible. When the Solar Orbiter, Wind, and STEREO spacecraft are in alignment, it is now possible to analyze the entire process of CME–CME interactions through in situ observations at various distances and angles. According to the different in situ signatures, the complex structures can be referred to as the complex ejecta (L. Burlaga 2002), the multiple magnetic clouds (MCs; Y. M. Wang et al. 2003b), and the shock-embedded MC (shock-MC), or shock-embedded ICME (shock-ICME) events (N. Lugaz et al. 2015; C. Shen et al. 2017). Using Solar Orbiter's in situ observations at 0.5 au, D. Trotta et al. (2024) reported a fast magnetosonic forward–reverse shock pair resulting from the interaction between two successive CMEs. By combining data from Wind in situ observations, it was observed that the intensities of such shock pairs tend to weaken with increasing heliocentric distance. C. Shen et al. (2018) present a quantitative analysis estimating that the geoeffectiveness of individual CMEs is amplified by approximately a factor of 2 due to shock–CME interactions near 1 au. One outstanding question is the fate of a shock as it propagates into an ICME, specifically whether it will dissipate during the interaction with CMEs (N. Lugaz et al. 2015). N. Lugaz et al. (2015) found most of these shocks are measured in the back half of a CME and concluded that about half the shocks may dissipate inside a CME before exiting it. The simulation results also show that if the shock is weak or slow enough, it may dissipate as it propagates into the region of higher magnetosonic speed inside the ICMEs (M. Xiong et al. 2006). Some studies suggest that shocks can completely traverse preceding CMEs, resulting in unique in situ signatures such as a shocked ICME entrained in the sheath between the shock and the host ejecta (ICME-in-sheath; Y. Chi et al. 2020; Y. D. Liu et al. 2020; C. Shen et al. 2021), or isolated but long-duration ICMEs with extremely dense sheath ahead of it (S. Dasso et al. 2009). However, it is challenging to determine which shock is associated with the following ICME and to identify the interplanetary sources of the two shocks.

In this work, we focus on the magnetic field evolution of a complex shock-ICME event detected by Solar Orbiter, Wind, and STEREO-A, corresponding to CMEs that erupted between 2023 November 27 and 28. During that time, the Solar Orbiter

and STEREO-A were positioned on opposite sides of the Wind spacecraft, with separation angles of $10°$ and $6°.4$ in heliographic longitude and separation distances of 0.16 and 0.02 au in radial distance, respectively. According to S. W. Good & R. J. Forsyth (2016), when two spacecraft are within $30°$ of each other, there is a 65% probability that they will detect the same ICME event. This alignment provides a valuable opportunity to study the evolution of the magnetic field during the interaction of ICMEs. The solar sources of the CMEs can be detected by the Hα Imaging Spectrograph (HIS; F. Cheng & L. Chuan 2022) on board the Chinese Hα Solar Explorer (CHASE; C. Li et al. 2022; Y. Qiu et al. 2022) and the Lyα Solar Telescope (LST; J. Zhao et al. 2022) on board the Advanced Space-based Solar Observatory (ASO-S; W.-Q. Gan et al. 2019). In Section 2, we present remote-sensing observations of the Sun, the solar corona, and in situ observations from Solar Orbiter, Wind, and STEREO-A and the analysis of the evolution of the shock–ICME interaction. The summary is presented in Section 3.

2. Event Analysis

The first CME (CME-1) was first detected by the coronagraph on board the Solar and Heliospheric Observatory (SOHO)/LASCO-C2 and STEREO-A/SECCHI-COR2 at 20:53:30 UT on November 27. Approximately 3 hr later, at 23:53 UT on November 27, the second CME (CME-2) appeared in the field of view (FOV) of SECCHI-COR2 and LASCO-C2. Figure 1 panel (a) shows the solar source of CME-2 from CHASE/HIS. Panel (b) shows the eruption of CME-2 in the inner coronagraph from ASO-S/LST. To obtain the 3D configuration of CME-1 and CME-2, we used the graduated cylindrical shell (GCS) model (A. Thernisien et al. 2006, 2009) to visually fit CMEs detected in the FOV of SECCHI-COR2 and LASCO-C3. The panels (e) and (f) in Figure 1 show the two CMEs (CME-1 and CME-2) at one instance, as observed by SECCHI-COR2 at 01:38 UT and LASCO-C3 at 01:42 UT on November 28, respectively. The purple and green wireframes in panels (i) and (j) show the best-fitting results of the GCS model for CME-1 and CME-2, respectively. CME-1 propagates along a latitude of $-14°.5$, a heliographic longitude of $-3°.2$, with a velocity of 901.57 km s^{-1}, while CME-2 propagates along a latitude of $-23°.0$, a heliographic longitude of $29°$, with a velocity of 1184.15 km s^{-1}. A direct impression is that CME-1 and CME-2 may interact with each other since their propagation directions are close to each other and the velocity of CME-2 is faster than that of CME-1. The radio burst detected from STEREO-A/WAVES shows a sudden enhancement of type II emission at decameter–hectometric wavelengths from 00:48 UT to 00:58 UT on November 28, as indicated by the white arrow in panel (d). The broadband enhancement, which occurred near 1.5 MHz with a bandwidth of 1 MHz, was produced by the interaction between CME-1 and CME-2. It is consistent with the clear overlaid shape between CME-1 and CME-2 detected in coronagraph images (panels (e), (f), (i), and (j)). About one day later, another halo CME was detected by STEREO-A/COR-2 and SOHO/LASCO-C2. CME-3 first appeared in the FOV of the coronagraph at 21:38 UT on November 28. The solar source of CME-3 can also be detected by CHASE/HIS, as shown in panel (c). The propagation direction of CME-3 is $2°$ in longitude and $-7°$ in latitude. The initial velocity of CME-3 is 1374.25 km s^{-1}, slightly faster than the velocity of CME-2,
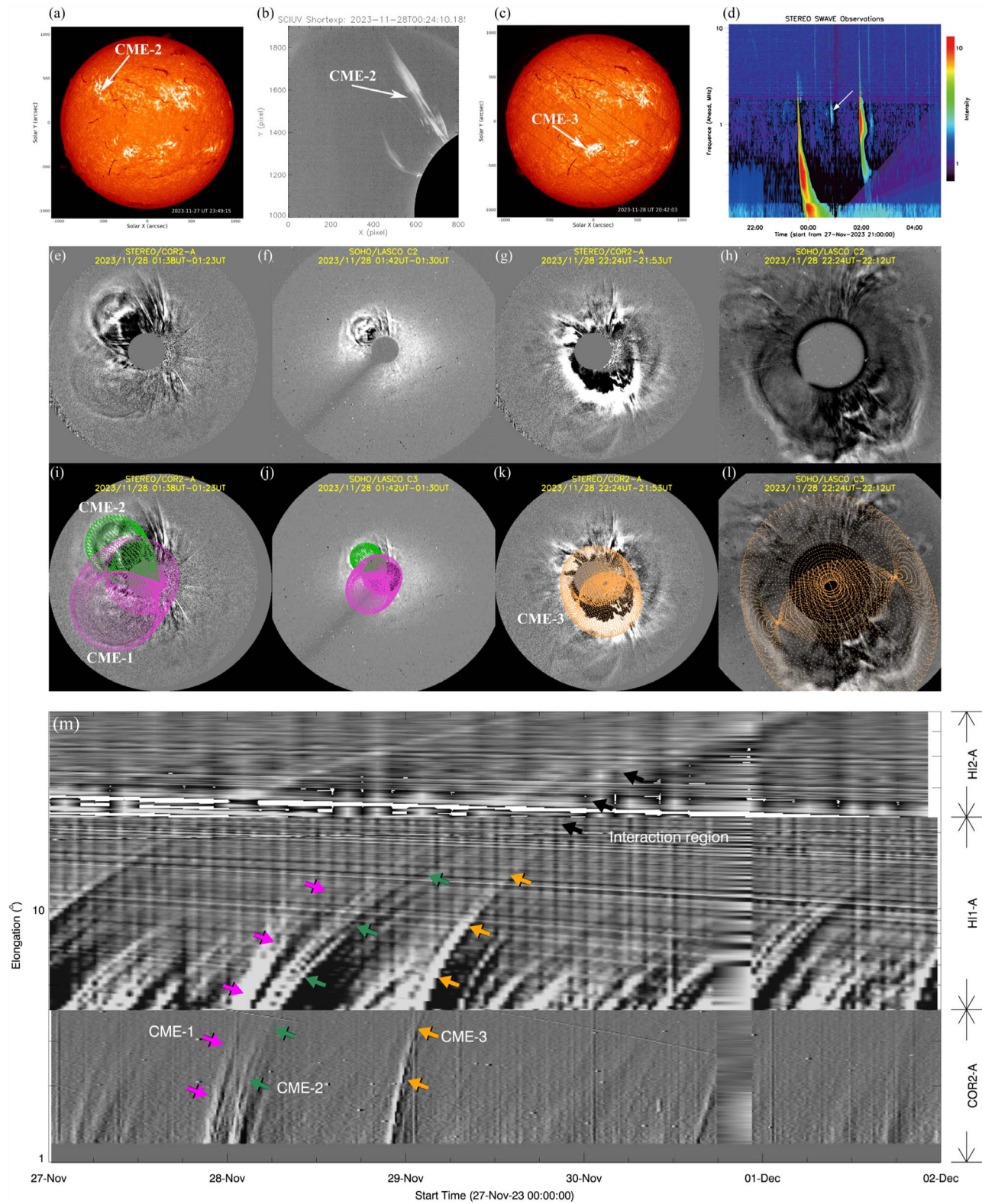
Figure 1. Panel (a) the full-Sun images at Hα line center (6562.8 Å) from CHASE spectroscopic observations at 23:49:15 UT on 2023 November 27. Panel (b) eruption of CME-2 in the inner corona detected by Lyα Solar Telescope (LST) on board the ASO-S. Panel (c) full-Sun images at Hα line center (6562.8 Å) from CHASE spectroscopic observations at 20:42:03 UT on 2023 November 28. Panel (d) STEREO-A radio dynamic spectrum associated with the interaction between CME-1 and CME-2. Panels (e)–(h) the running difference images of the three CMEs detected by STEREO-A/SECCHI and SOHO/LASCO on 2023 November 28. Panels (i)–(l) are the best-fitting results for the three CMEs. The purple, green, and yellow meshes display the results of the GCS fitting for CME-1, CME-2, and CME-3, respectively. Panel (m) shows the time-elongation map derived from the COR2, HI1, and HI2 cameras on board STEREO-A. The purple, green, and yellow arrows indicate the tracks of CME-1, CME-2, and CME-3, respectively. The black arrows show the potential interaction region based on the merged track.
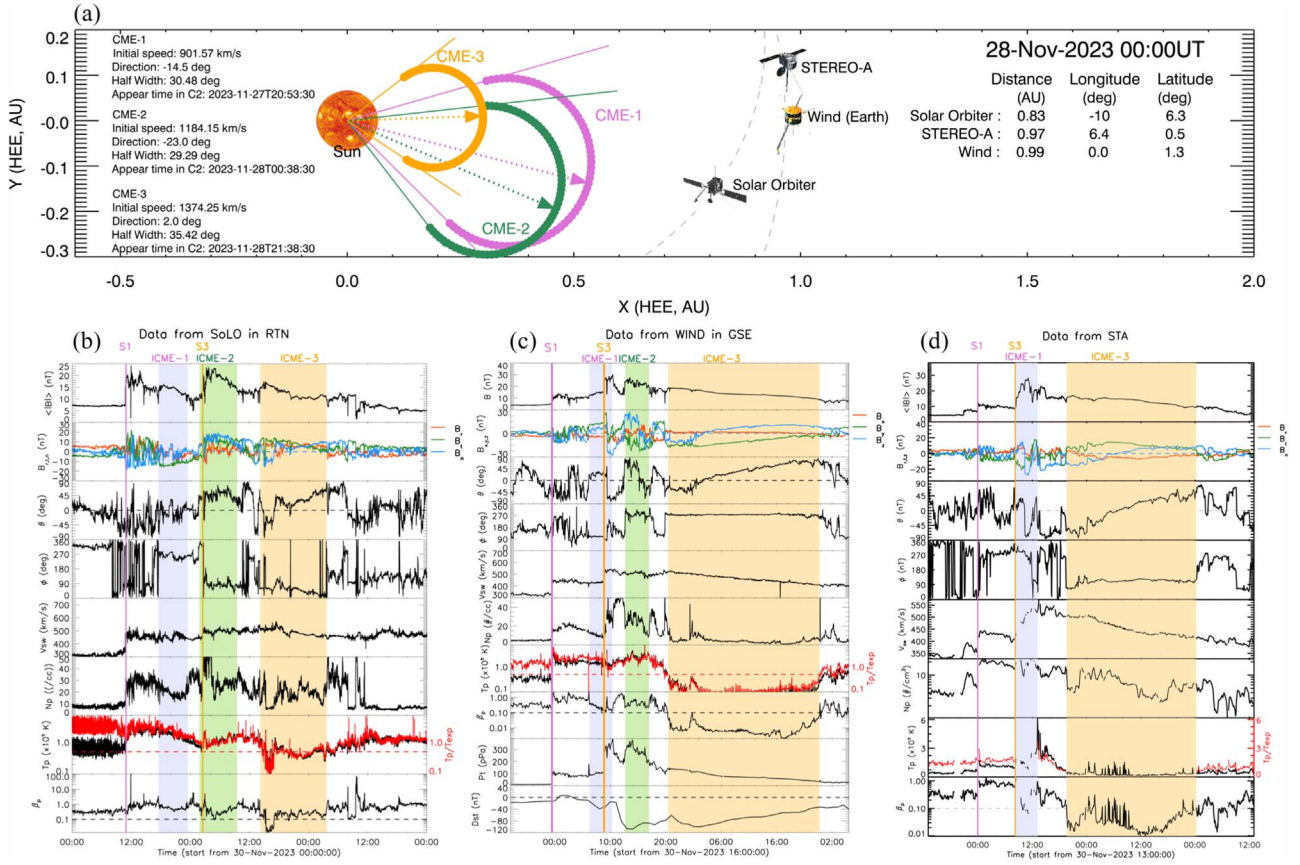
Figure 2. Panel (a): the positions of three separated spacecraft (Wind, Solar Orbiter, and STEREO-A) at 00:00 UT on 2023 November 28, in the inner heliosphere. The purple, green, and yellow arrows represent the reconstructed propagation direction of the three CMEs from the GCS model, respectively. The circles represent the half angular width of the CMEs derived from the GCS model. Panels (b)–(d): solar wind plasma and magnetic field parameters detected at Solar Orbiter, Wind, and STEREO-A spacecraft. From top to bottom, the panels show the magnetic field strength, the r, t, and n magnetic field components in RTN coordinate, the elevation θ and azimuth ϕ of field direction in RTN coordinate, bulk speed, proton density, proton temperature, proton β, total pressure (only in panel (c)), and Dst index (only in panel (c)), respectively. The purple, green, and yellow shade regions show the intervals of ICME-1, ICME-2, and ICME-3, respectively. The purple vertical line indicates the arrival time of shock-1, which is associated with ICME-1. The yellow dashed vertical line indicates the arrival time of shock-3, which is associated with ICME-3.

which indicates that CME-3 may chase and interact with CME-2 at a large distance from the Sun. The tracks of the three CMEs can be traced using time-elongation maps (J-maps) derived from data from STEREO-A/COR-2, HI-1, and HI-2. The purple, green, and yellow arrows represent the trajectories of CME-1, CME-2, and CME-3, respectively. Although CME-1 and CME-2 exhibit clear signs of interaction in the FOV of COR-2, their tracks in the ecliptic plane J-map show no significant overlap. This suggests that, due to their differing propagation directions, the interaction between the two CMEs in the ecliptic plane is relatively weak. This may explain why CME-1 and CME-2 can be distinguished in in situ observations. The J-map reveals a distinct merging of CME-2 and CME-3 at an elongation angle of approximately 30°, indicating an interaction between these two CMEs during their propagation. It indicates that CME-3 may catch up with CME-2 before reaching the Solar Orbiter.

2.1. Interaction between CMEs

Figure 2 panel (a) shows the position of the Wind (Earth), STEREO-A, and Solar Orbiter in the ecliptic plane on 2023 November 28. The detailed information of the three spacecraft is listed in Table 1. The central propagation directions of the three CMEs, determined by the GCS model, are also shown in

panel (a) by purple, green, and yellow arrows, respectively. The circles represent the angular widths of the CMEs derived from the GCS model. Assuming radial propagation of the CMEs, the spacecraft in situ measurements have a greater than 69% chance of detecting the CMEs, if the half angular width of the CME is greater than the angle between the central propagation angle of the CME and the spacecraft (Z. Zhong et al. 2021). According to this criterion, we extrapolated that CME-1 and CME-3 can be detected by all three spacecraft (STEREO-A, Wind, and Solar Orbiter), whereas CME-2 can only be detected by two spacecraft (Wind and Solar Orbiter). Due to the potential formation of complex structures from interactions between three successive CMEs, we labeled the ICME events detected by in situ in chronological order as ICME-1, ICME-2, and ICME-3. The corresponding shocks generated by these CMEs were then labeled S1, S2, and S3. Since no clear shock associated with ICME-2 was detected in the in situ data, there will be no reference to S2 hereafter.

Figure 2 panel (b) shows the in situ observations detected by Solar Orbiter spacecraft from 2023 November 30 to December 2. From top to bottom, the panels display the magnetic field strength, the r, t, and n magnetic field components in RTN coordinate, the elevation θ and azimuth ϕ of field direction in RTN coordinate, bulk speed, proton density, proton temperature, and proton β, respectively. As shown in panel (b), three

Table 1
ICME Properties at Solar Orbiter, Wind, and STEREO-A for 2023 November 20 to December 4

	Parameters	Unit	Solar Orbiter	Wind	STEREO-A
ICME-1	$T_{\mathrm{shock-1}}$	UT	2023-11-30T10:55:00	2023-11-30T23:27:08	2023-11-30T23:55:42
	T_{begin}	UT	2023-11-30T17:40:00	2023-12-01T06:14:17	2023-12-01T08:13:17
	T_{end}	UT	2023-11-30T23:30:00	2023-12-01T10:17:08	2023-12-01T13:08:34
	$\triangle_T$	hr	5.83	4.03	4.92
	$B_{\mathrm{max}}/B_{\mathrm{mean}}$	nT	16.25/13.90	28.60/18.23	28.17/20.81
ICME-2	$T_{\mathrm{shock-2}}$	UT	…	…	…
	T_{begin}	UT	2023-12-01T01:50:00	2023-12-01T12:40:00	…
	T_{end}	UT	2023-12-01T09:30:00	2023-12-01T16:57:08	…
	$\triangle_T$	hr	7.67	4.28	…
	$B_{\mathrm{max}}/B_{\mathrm{mean}}$	nT	23.54/17.90	27.68/22.74	…
ICME-3	$T_{\mathrm{shock-3}}$	UT	2023-12-01T02:26:00	2023-12-01T08:51:25	2023-12-01T08:13:17
	T_{begin}	UT	2023-12-01T14:10:00	2023-12-01T20:24:17	2023-12-01T19:34:17
	T_{end}	UT	2023-12-02T03:40:00	2023-12-02T23:40:08	2023-12-03T00:16:25
	$\triangle_T$	hr	13.50	27.25	28.70
	$B_{\mathrm{max}}/B_{\mathrm{mean}}$	nT	17.44/12.38	18.93/13.78	16.89/13.40
Position	R	AU	0.83	0.99	0.97
	Lon	deg	−10	0.0	6.4
	Lat	deg	6.3	1.3	0.5

corresponding CMEs were all detected by the Solar Orbiter. The spacecraft detected the leading edge of ICME-1 at 17:40 UT on 2023 November 30, and the trailing edge at 23:30 UT on 2023 November 30 (indicated by the purple-shaded region). The corresponding shock (S1), marked by the purple vertical line, arrived at the Solar Orbiter on 2023 November 30, at 10:55 UT, about 7 hr before the leading edge of ICME-1. The in situ measurements during the purple-shaded region showed enhanced magnetic field intensity, low plasma density, and decreasing velocity. The relatively higher proton temperature and plasma β indicate an interaction between ICME-1 and ICME-2, consistent with the white-light observations from coronagraphs. Approximately 2 hr later, the second ICME (ICME-2, indicated by the green-shaded region) was detected. ICME-2 started at 01:50 UT and ended at 09:30 UT on December 1, with a duration of ∼8 hr. ICME-2 was characterized by a strong interplanetary shock (hereinafter S3, denoted by the yellow vertical line) propagating through its structure. The shock, which was most likely caused by CME-3, was detected at 2:30 UT on December 1, about 40 minutes after the arrival of ICME-2. S3 compressed the ICME-2, resulting in a significant increase in magnetic field, velocity, and proton density. The source of S3 (hereinafter ICME-3, represented as the yellow shade region) was found approximately 4.6 hr later with enhancement magnetic fields, rotation of the field vector, low proton temperature, low plasma β, and decreasing velocity. The in situ observations presented the typical characteristics of shocks propagating inside preceding ejecta, resulting in a shock–ICME complex structure. Regions with lower magnetic field intensity, enhanced plasma density, and enhanced plasma β are observed between ICME-1, ICME-2, and ICME-3, indicating the interaction and compression between them (Y. M. Wang et al. 2003b). Overall, from November 30 to December 2, three ICMEs and two shocks were identified from the observations of Solar Orbiter. The detailed information is listed in Table 1. Based on the arrival times of the ICMEs detected by the Solar Orbiter, we infer that they correspond to the interplanetary structures of the CMEs that erupted on 2023 November 27–28.

Panel (c) shows in situ observations detected by Wind spacecraft. The shock (S1) driven by ICME-1 arrived at Earth at 23:27 UT on November 30. Approximately 7 hr later, the leading edge of ICME-1 arrived at Wind at 06:14 UT on December 1. The first half of the event is characterized by an enhanced magnetic field, smoothly changing magnetic field directions, relatively low density, and low plasma β. At 08:51 UT on December 1, a fast forward shock (indicated by a yellow vertical line) was detected propagating inside ICME-1, showing a sudden enhancement in magnetic field, velocity, plasma density, and total pressure. The trailing edge of ICME-1 was identified around 10:17 UT, determined from a decrease in magnetic field, and an increase in plasma β and temperature, which is very similar to the interaction region between two CMEs as described in Y. M. Wang et al. (2003b). About 2.5 hr later, the ICME-2 was detected by Wind spacecraft from 12:40 UT to 16:57 UT on December 1. The ICME-3 (shown by the yellow shade region) started at 20:24 UT on December 1, lasting about 27 hr, and ended at 23:40 UT on December 2. The duration of ICME-2 is usually short with relative strong magnetic field and plasma density, indicating that ICME-2 is entrained in the sheath between S3 and ICME-3 (Y. D. Liu et al. 2020). This is consistent with observations from Solar Orbiter, which did not detect a shock associated with ICME-2 but did observe a clear shock driven by ICME-3 passing through ICME-2. Thus, we believe the source of S3 is ICME-3. Between the Solar Orbiter at 0.83 au and the Wind spacecraft at 1 au, S3 has completely passed through ICME-2 and entered the interior of ICME-1. The D_{st} index decreases in three stages. Initially, there is a clear decrease during the interval of ICME-1, followed by a recovery to normal values. The D_{st} index then rapidly decreases again between ICME-1 and ICME-2 due to the shock's compression of the southward component of the magnetic field. On November 1, 2023, at 14:00 UT, the D_{st} index reached a peak of −108 nT. After this peak, the D_{st} index recovered and subsequently decreased once more as ICME-3 arrived at Earth.

In situ observations from STEREO-A spacecraft from 13:00 UT on November 30 to 12:00 UT on December 3 are

Table 2
Shock Times and Parameters for S3 at Solar Orbiter, Wind, and STEREO-A

Spacecraft	Shock Time (UT)	$\langle \hat{n}_{RTN} \rangle$	$\langle \theta_{Bn} \rangle$ (deg)	$\langle r_B \rangle$	$\langle r \rangle$	$\langle v_{sh} \rangle$ (km s^{-1})	M_{fms}	M_A
Solar Orbiter	2023-12-01T02:26:00	[0.98, 0.001, −0.21]	61.9	1.74	2.42	548.69	1.32	2.09
Wind	2023-12-01T08:51:25	[−0.91, 0.330, −0.24]	50.0	1.59	1.53	555.73	0.99	1.20
STEREO-A	2023-12-01T08:13:17	⋯	⋯	1.49	⋯	⋯	⋯	⋯

shown in Figure 2 panel (d). ICME-2 may have missed STEREO-A, due to the angular width of CME-2 being less than the separation angle between the propagation direction of CME-2 and STEREO-A. As a result, only two shocks and two ICMEs were detected by STEREO-A. S1 arrived at STEREO-A at 23:55 UT on November 30. About 8.3 hr later, ICME-1 (purple-shaded region) was detected from 08:13 UT to 13:08 UT on December 1, lasting about 5 hr. The leading and trailing boundaries of ICME-1 were determined from the enhancement of the magnetic field, lower plasma β, and lower temperature. A clear forward shock (S3, marked by a yellow vertical line) passed STEREO-A at 08:13 UT on December 1, indicating that S3, driven by ICME-3, was overtaking the preceding ICME-1 at STEREO-A. Due to the shock compression, the magnetic field data of ICME-1 show a clear enhancement, with the average magnetic field intensity reaching 20.81 nT. The velocity of ICME-1 also shows a clear increase due to the compression from S3 and ICME-3. ICME-3 arrived at STEREO-A at 19:34 UT on December 1 and lasted for about 29 hr (yellow-shaded region). ICME-3 is a typical ICME, evidenced by its smoothly changing magnetic field direction, decreasing velocity, reduced temperature, and plasma β.

Based on in situ observations from three different locations, we identified that S3 propagated through both ICME-2 and ICME-1 as it traveled from Solar Orbiter to 1 au. A comparison of S3's properties at Solar Orbiter, Wind, and STEREO-A is crucial for understanding the complex interactions between the shock and the ICMEs. The shock parameters are obtained by nonlinear least-squares fitting of the incomplete Rankine–Hugoniot relations (temperature information is not used) originally developed by A. F. Viñas & J. D. Scudder (1986) and further enhanced by A. Szabo (1994). As noted by D. Trotta et al. (2022), the choice of upstream/downstream averaging windows is crucial for accurately estimating shock parameters. In this work, we use a 4 minute window to obtain the parameters, which falls within the typical range used for interplanetary shock studies. The parameters of S3 are presented in Table 2, including time, shock normal direction ($\hat{n}$), shock normal vector (θ_{Bn}), magnetic compression ratio (r_B), density compression ratio (r), shock speed (v_{sh}), fast magnetosonic Mach numbers (M_{fms}), and Alfvénic Mach numbers (M_A). For STEREO-A, due to a data gap in plasma measurements after the arrival of S3, we were unable to obtain complete shock parameters. In these parameters, Mach number, density, and magnetic compression ratio serve as indicators of shock strength. From Solar Orbiter to 1 au, the intensity of the shock weakened significantly, as indicated by the magnetic compression ratio decreasing from 1.74 at Solar Orbiter to 1.59 at Wind, and further to 1.49 at STEREO-A. In addition to the decreasing magnetic compression ratio, the fast magnetosonic Mach numbers, Alfvénic Mach numbers (M_A), and density compression ratio of S3 also show significant reductions, further indicating a weakening of the shock's strength during

its propagation. The fitted normal direction of S3 at Solar Orbiter is [0.98, 0.001, −0.21] in RTN coordinates, and it is [−0.91, 0.330, −0.24] at Wind. This significant change in the normal direction of S3 may be attributed to its interaction with ICME-1 and ICME-2 during propagation. The forward shock is oblique at Solar Orbiter, with $\theta_{Bn} \sim 61°9$, and at Wind, with $\theta_{Bn} \sim 50°0$, indicating that the shock's orientation relative to the upstream magnetic field remained oblique during its propagation. The velocity of S3 at Solar Orbiter is 548.69 km s^{-1}, which aligns closely with Wind's measured velocity of 555.73 km s^{-1}. In summary, S3 is fast but relatively weak compared to the average shock parameters at 1 au (E. K. J. Kilpua et al. 2015). It is consistent with the statistical findings of N. Lugaz et al. (2015), where the shock's strength decreases rapidly due to the high upstream Alfvén speeds.

2.2. Radial Evolution

The small longitudinal (within $10°$) and latitudinal separation between Solar Orbiter, Wind, and STEREO-A during the passage of the ICME provides an opportunity to study the radial evolution of magnetic field during the interaction between shock and CMEs. Figure 3 displays the magnetic field observations from Solar Orbiter (blue), Wind (black), and STEREO-A (red). From top to bottom, Figure 3 shows the total magnetic field intensity ($|B|$), three components of the magnetic field in the RTN coordinate system, the elevation θ, and azimuth ϕ of field direction in RTN coordinate from Wind, Solar orbiter, and STEREO-A. The start and end times of ICME-1, ICME-2, and ICME-3 are given in Table 1.

Panel (a) shows the Solar Orbiter, Wind, and STEREO-A observations for ICME-1. To align the arrival time of ICME-1, the observations from Solar Orbiter were shifted back by 12.452 hr, and those from STEREO-A were moved forward by 2.3 hr, without stretching or compressing. The black, red, and blue vertical dotted–dashed lines indicate the end time of the ICME-1 detected by Wind, STEREO-A, and Solar Orbiter, respectively. As shown in panel (a), the magnetic field intensities detected by Wind (black) and STEREO-A (red) are much higher than those detected by Solar Orbiter (blue). At Solar Orbiter, the maximum and average magnetic field intensities of ICME-1 are 16.26 and 13.90 nT, respectively, without any obvious compression by the following shock S3. Assuming ICME-1 is self-expanding, the maximum and average magnetic field intensities at 1 au should be 11.19 and 9.58 nT, respectively. According to the in situ observations, the maximum and average magnetic field intensities at Wind are 28.60 and 18.23 nT, and at STEREO-A they are 28.17 and 20.81 nT, respectively. The abnormal enhancement (152%–156% for maximum intensity and 90.0%–117.2% for mean intensity) of the magnetic field in ICME-1 at 1 au is due to the compression by the shock. The lengths of ICME-1 at Wind and STEREO-A are 4.03 and 4.92 hr, respectively, which are significantly shorter than the duration of ICME-1 (5.83 hr)
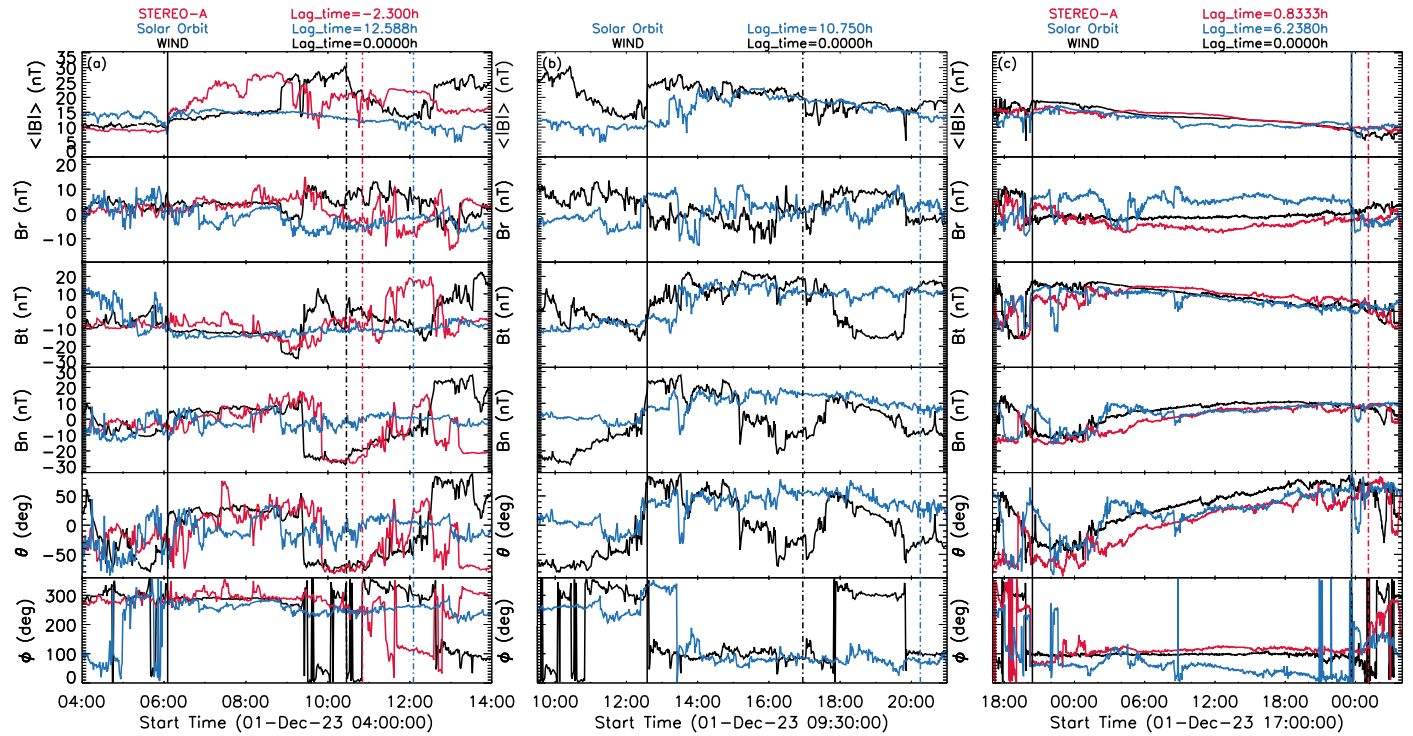
Figure 3. In situ observations for ICME-1 (left panels), flux rope (middle panels), and ICME-2 (right panels). From top to bottom, the panels display the magnetic field strength, the r, t, and n magnetic field components in RTN coordinate, the elevation θ, and the azimuth ϕ of field direction in RTN coordinate. The black, red, and blue lines in the field data panels correspond to the observations from Wind, STEREO-A, and Solar Orbiter, respectively. The STEREO-A and Solar Orbiter observations are time-shifted to align with the start times of the structures. The black, red, and blue vertical dotted–dashed lines indicate the end time of the ICMEs detected by Wind, STEREO-A, and Solar Orbiter, respectively. The observations from Solar Orbiter in panel (c) are scaled to match the interval of ICME-2 detected at WIND.

identified by Solar Orbiter. The compression by S3 at Wind and STEREO-A is also the primary cause of the reduced interval of ICME-1. Despite the complex interactions, the magnetic field profiles at Wind, STEREO-A, and Solar Orbiter appear similar, as shown in panel (a).

ICME-2 was only detected by Solar Orbiter and Wind as shown in Figure 3 panel (b). To align the arrival time of ICME-2, the observations from the Solar Orbiter were shifted back by 10.750 hr. At Solar Orbiter, S3 was within ICME-2, and the magnetic field intensity in the back half of ICME-2 was clearly enhanced. By the time ICME-2 reached Wind, S3 had already passed through it. The maximum and mean magnetic field intensities of ICME-2 at Wind were 27.68 and 22.74 nT, slightly higher than those detected at Solar Orbiter (23.54 and 17.90 nT). The black and blue vertical dashed–dotted lines indicate the trailing boundary of ICME-2 at Wind and Solar Orbiter, respectively. The interval of ICME-2 at Wind was 4.28 hr, approximately 55.8% shorter than the 7.67 hr at Solar Orbiter. In addition to the compression from S3, further compression from ICME-3 might account for ICME-2's shorter interval at Wind.

Figure 3 panel (c) shows the interval of ICME-3 detected by Solar Orbiter (blue), Wind (black), and STEREO-A (red). To align the arrival time of ICME-3, the observations from the Solar Orbiter were shifted back by 6.238 hr, and those from STEREO-A were moved forward by 0.8333 hr. The Solar Orbiter observations were stretched to match the duration of ICME-3 detected at Wind for a better comparison of the magnetic field vectors. The maximum and mean magnetic field intensities of ICME-3 detected by the Wind spacecraft are slightly higher than those detected by STEREO-A and Solar

Orbiter. Despite the differences in intensity, the magnetic field vectors exhibit similar rotations across all three components at each spacecraft.

Figure 4 presents direct evidence of the shock passing through two preceding ICMEs. From top to bottom, it shows the magnetic field intensity detected by Solar Orbiter, Wind, and STEREO-A. The arrival times of S1 at Solar Orbiter, Wind, and STEREO-A were aligned by shifting the observations from Solar Orbiter back by 24.535 hr and those from STEREO-A forward by 0.476 hr. The in situ data from Solar Orbiter, Wind, and STEREO-A clearly show the complete path of the shock caused by ICME-3, which propagated into ICME-2 at Solar Orbiter, passed through ICME-2 from 0.86 to 1 au, then propagated into ICME-1 at Wind, and finally passed through ICME-1 at STEREO-A. The right panels in Figure 4 illuminate the whole process of the shock driven by ICME-3 passed through the two preceding CMEs. The interaction between the shock and the ICMEs results in a significant increase in the magnetic field strength in both ICME-1 and ICME-2. Despite the small longitudinal separation (6°.4) and distance (0.02 au) between Wind and STEREO-A, the different propagation directions of the CMEs and the interactions between them may still result in distinct differences in their in situ observations.

3. Summary

In this work, we investigated a complex shock–CME interaction event by combining HIS observations from the CHASE spacecraft, low coronal data from ASO-S/LST, and coronagraph data from SOHO/LASCO and STEREO/SEC-CHI with in situ measurements from Solar Orbiter, Wind, and STEREO-A, presenting direct evidence of a forward shock
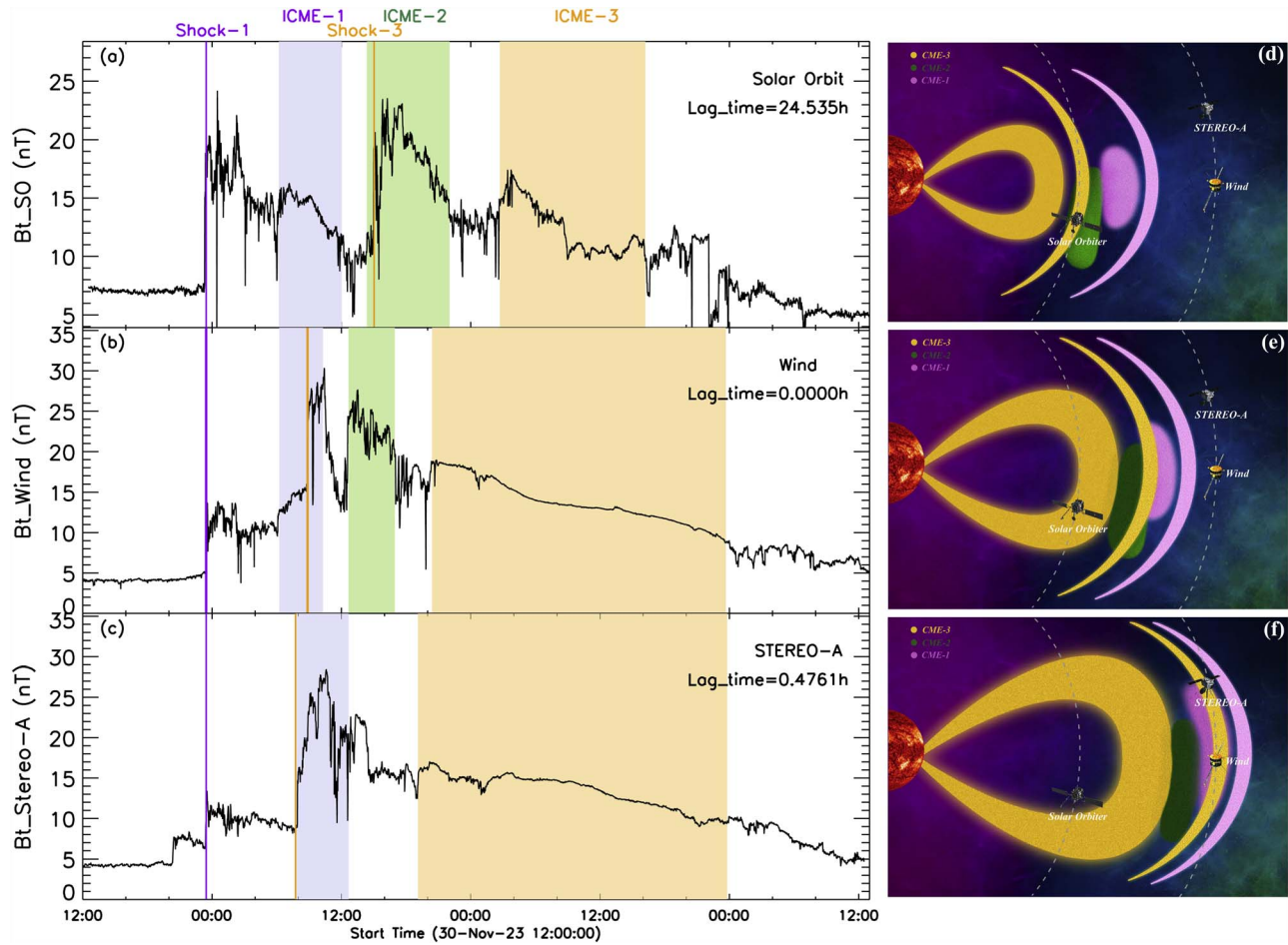
Figure 4. Panels (a)–(c) show the magnetic field strength detected by Solar Orbiter, Wind, and STEREO-A, respectively. The purple and yellow vertical lines indicate the arrival time of S1 and S3, respectively. The purple, green, and yellow shade regions show the intervals of ICME-1, ICME-2, and ICME-3, respectively. The illustrations on the right present the whole process of the shock driven by ICME-3 passed through the two preceding CMEs: panel (d) shows the relative positions of two shocks and three ICMEs at Solar Orbiter, panel (e) shows the relative positions of two shocks and three ICMEs between 0.86 and 1 au, and panel (f) shows the relative positions of two shocks and three ICMEs at 1 au. We also provide an animation for panels (d)–(e) to illustrate the entire process of the shock traversing preceding two CMEs. The real-time duration of the animation is 5 s.

(An animation of this figure is available in the online article.)

passing through two preceding ICMEs. The complex shock–CME interaction event was caused by the interplanetary interaction of three consecutive CMEs on November 27–28. Based on the eruption times of the three CMEs, as well as the propagation direction and initial velocity obtained from the GCS model, we infer that CME-1 and CME-2 have interacted with each other at a distance near the solar surface, and CME-3 have sequentially chased and interacted with CME-2 and CME-1 at far distance from the Sun.

Connections with in situ observations detected at Solar Orbiter suggest that three corresponding ICMEs clearly interacted with each other. The shock (S3) driven by ICME-3 propagated into ICME-2 at Solar Orbiter, indicating the interaction between ICME-2 and ICME-3 started before 0.83 au. According to Wind in situ observations, S3 driven by ICME-3 has passed through ICME-2 and propagated into the ICME-1 at 1 au. Using in situ data from Solar Orbiter, Wind, and STEREO-A, the entire process of ICME-1 and ICME-2 being significantly compressed by S3 is presented. The intensity of S3 weakened significantly from Solar Orbiter to 1 au, as indicated by the decrease in magnetic compression ratios, density compression ratios, fast magnetosonic Mach numbers, and Alfvénic Mach numbers. The normal direction of

S3 showed a significant change, which may be attributed to its interaction with ICME-1 and ICME-2 during propagation. The maximum magnetic field intensity of ICME-1 is enhanced by approximately 152%–156% due to the compression of S3 from Solar Orbiter to Wind. Despite a 16°.4 difference in the in situ observation position, CME-3, which has a large angular width and shows no obvious interaction, maintains essentially the same internal magnetic field structure.

This work presents a detailed case study of a shock propagating into two preceding ICMEs, shedding light on the impact of shock–CME interactions on both shock intensity and ICME compression. These findings demonstrate that the compression of ICMEs by subsequent shocks can significantly amplify the magnetic field strength, which may have significant implications for space weather. As we approach the solar maximum of Solar Cycle 25, such interactions are expected to occur more frequently. A more thorough understanding of shock–CME interactions is essential for improving space weather forecasting, particularly for predicting severe geomagnetic storms. In the future, data from new missions in the inner heliosphere, such as Solar Orbiter and Parker Solar Probe, combined with observations from Wind, STEREO, and even more distant missions like MAVEN and Tianwen-1, will be

critical for advancing our understanding of shock–CME interactions.

Acknowledgments

ORCID iDs

Yutian Chi ● https://orcid.org/0000-0001-9315-4487
Chenglong Shen ● https://orcid.org/0000-0002-3577-5223
Mengjiao Xu ● https://orcid.org/0000-0002-2924-7520
Junyan Liu ● https://orcid.org/0009-0006-7051-0438
Can Wang ● https://orcid.org/0000-0002-2865-4626
Bingkun Yu ● https://orcid.org/0000-0003-2758-1960
Zhihui Zhong ● https://orcid.org/0000-0002-5627-2377
Yuming Wang ● https://orcid.org/0000-0002-8887-3919

References

Burlaga, L. F., Behannon, K. W., & Klein, L. W. 1987, JGRA, 92, 5725
Burlaga, L., Plunkett, S., & St. Cyr, O. 2002, JGRA, 107, 1266
Cheng, F., & Chuan, L. 2022, ChJSS, 42, 546
Chi, Y., Shen, C., Wang, Y., et al. 2016, SoPh, 291, 2419
Chi, Y., Scott, C., Shen, C., et al. 2020, ApJ, 899, 143
Chi, Y., Scott, C., Shen, C., et al. 2021, ApJL, 917, L16
Dasso, S., Mandrini, C. H., Schmieder, B., et al. 2009, JGRA, 114, A2
Gan, W.-Q., Zhu, C., Deng, Y.-Y., et al. 2019, RAA, 19, 156
Good, S. W., & Forsyth, R. J. 2016, SoPh, 291, 239
Gopalswamy, N., Yashiro, S., Kaiser, M. L., Howard, R. A., & Bougeret, J.-L. 2001, ApJ, 548, L911
Gopalswamy, N., Yashiro, S., Liu, Y., et al. 2005, JGRA, 110, A09S15
Kaiser, M. L., Kucera, T. A., Davila, J. M., et al. 2008, SSRv, 136, 5
Kilpua, E. K. J., Lumme, E., Andreeova, K., Isavnin, A., & Koskinen, H. E. J. 2015, JGRA, 120, 4112
Li, C., Fang, C., Li, Z., et al. 2022, SCPMA, 65, 289602
Liu, Y. D., Chen, C., & Zhao, X. 2020, ApJL, 897, L11
Liu, Y. D., Luhmann, J. G., Möstl, C., et al. 2012, ApJL, 746, L15
Lugaz, N., Farrugia, C. J., Davies, J. A., et al. 2012, ApJ, 759, 68
Lugaz, N., Farrugia, C. J., Smith, C. W., & Paulson, K. 2015, JGRA, 120, 2409
Lugaz, N., Temmer, M., Wang, Y., & Farrugia, C. J. 2017, SoPh, 292, 64
Lugaz, N., Vourlidas, A., Roussev, I. I., & Morgan, H. 2009, SoPh, 256, 269
Mishra, W., Srivastava, N., & Chakrabarty, D. 2015, SoPh, 290, 527
Müller, D., Cyr, O. S., Zouganelis, I., et al. 2020, A&A, 642, A1
Qiu, Y., Rao, S., Li, C., et al. 2022, SCPMA, 65, 289603
Scolini, C., Chané, E., Temmer, M., et al. 2020, ApJS, 247, 21
Shen, C., Chi, Y., Wang, Y., Xu, M., & Wang, S. 2017, JGRA, 122, 5931
Shen, C., Chi, Y., Xu, M., & Wang, Y. 2021, FrP, 9, 762488
Shen, C., Xu, M., Wang, Y., Chi, Y., & Luo, B. 2018, ApJ, 861, 28
Shen, C., Wang, Y., Wang, S., et al. 2012, NatPh, 8, 923
Szabo, A. 1994, JGRA, 99, 14737
Temmer, M., Veronig, A. M., Peinhart, V., & Vršnak, B. 2014, ApJ, 785, 85
Thernisien, A., Howard, R., & Vourlidas, A. 2006, ApJ, 652, 763
Thernisien, A., Vourlidas, A., & Howard, R. A. 2009, SoPh, 256, 111
Trotta, D., Dimmock, A. P., Blanco-Cano, X., et al. 2024, ApJL, 971, L35
Trotta, D., Hietala, H., Horbury, T., et al. 2023, MNRAS, 520, 437
Trotta, D., Vuorinen, L., Hietala, H., et al. 2022, FrASS, 9, 1005672
Viñas, A. F., & Scudder, J. D. 1986, JGRA, 91, 39
Wang, Y., Ye, P., Wang, S., & Xue, X. 2003a, GeoRL, 30, 20
Wang, Y. M., Ye, P. Z., & Wang, S. 2003b, JGRA, 108, 1370
Wu, C.-C., & Lepping, R. P. 2011, SoPh, 269, 141
Xiong, M., Zheng, H., Wang, Y., & Wang, S. 2006, JGRA, 111, A08105
Yashiro, S., Gopalswamy, N., Michalek, G., et al. 2004, JGRA, 109, A7
Zhao, J., Zhang, P., Gibson, S., et al. 2022, A&A, 665, A39
Zhong, Z., Shen, C., Mao, D., et al. 2021, Univ, 7, 361
Zurbuchen, T. H., & Richardson, I. G. 2006, SSRv, 123, 31